Robustness of a persistent spin helix against a cubic Dresselhaus field in (001) and (110) oriented two-dimensional electron gases

D. Iizasa,[1] D. Sato,[1] K. Morita,[2] J. Nitta,[1,3,4] and M. Kohda[1,3,4,*]

[1]*Department of Materials Science, Tohoku University, Sendai 980-8579, Japan*
[2]*Graduate School of Electrical and Electronic Engineering, Chiba University, Chiba 263-8522, Japan*
[3]*Center for Spintronics Research Network, Tohoku University, Sendai 980-8577, Japan*
[4]*Center for Science and Innovation in Spintronics (Core Research Cluster), Tohoku University, Sendai 980-8577, Japan*

The persistent spin helix (PSH) state in III–V semiconductor quantum wells (QWs) is a promising candidate for spin-based applications because the PSH state realizes controllable spin orientation with long spin lifetime. Although the cubic Dresselhaus spin-orbit (SO) interaction is known for breaking the PSH state in both (001)-oriented and (110)-oriented QWs, it is not well understood how the distinct symmetry of cubic Dresselhaus terms β_3 between (001) and (110) QWs affects the robustness of the PSH state. Here we investigate robustness of the PSH state between (001) and (110) QWs under various strengths of cubic Dresselhaus SO interaction based on numerical Monte Carlo approach and magnetoconductance simulation, respectively, representing optical spin excitation/detection and weak localization/weak antilocalization in magnetotransport. For electron spins initialized along $z \parallel [001]$ in a (001) QW and $x \parallel [001]$ and $y \parallel [1\bar{1}0]$ in a (110) QW, where the spin distribution is developed with the helical spin mode, a (001) QW shows a more robust PSH state against the increase of β_3 than does a (110) QW. This phenomenon is contrary to numerically computed magnetoconductance, where weak localization is maintained on the variation of β_3 in a (110) QW, whereas weak antilocalization appears in a (001) QW. By deriving the spin lifetime of the PSH state in a (110) QW from a diffusion equation using a random-walk approach, we demonstrate that such a difference arises directly from the magnitude and orientation of third angular harmonics in cubic Dresselhaus fields for (001) and (110) QWs.

I. INTRODUCTION

Controlling spin states in a solid state is a fundamental requirement for realizing spintronic devices and for future quantum computing. In III–V semiconductor heterostructures such as GaAs/AlGaAs, spin-orbit (SO) interactions of two types exist: Dresselhaus SO interaction [1] induced by bulk inversion asymmetry of zinc-blende structure and Rashba SO interaction [2] induced by structural inversion asymmetry of a quantum well (QW). Both SO interactions induce effective magnetic fields for moving electrons, which enables us to generate and manipulate spin states in semiconductors electrically [3–6]. However, spin randomization is induced simultaneously because of the momentum-dependent SO fields. This so-called D'yakonov-Perel' spin relaxation plays a prominent role in losing spin information in III–V semiconductors [7]. Therefore, simultaneous realization of spin manipulation and long spin transport has been a challenging issue under the existence of SO interactions.

To overcome this obstacle, the persistent spin helix (PSH) state has been proposed theoretically [8,9]. The SO field is aligned in a uniaxial direction satisfying SU(2) symmetry [9], which creates a robust spin state against all forms of spin independent scattering. Such a PSH condition can be implemented in two crystal orientations in III–V semiconductor heterostructures. In a (001)-grown QW, equal strengths of Rashba and linear Dresselhaus SO fields enable the uniaxial SO fields to point to the QW plane. In a (110)-grown QW, the linear Dresselhaus SO field creates the PSH state with the SO field pointing perpendicularly to the QW plane. Figures 1(a) and 1(d), respectively, portray the effective magnetic fields $\boldsymbol{B}_1^{(001)}$ and $\boldsymbol{B}_1^{(110)}$, which form the PSH states in (001) and (110) QWs. Once the spin orientation is initialized along the z direction in a (001) QW, a helical spin mode is evolved [Fig. 1(b)] and long spin transport as well as controllable spin orientation are achieved simultaneously. The same situation for the in-plane spin orientation is implemented in the case of a (110) QW, as presented in Fig. 1(e). Consequently, the PSH state in (001) and (110) QWs has potential for realizing spin functionalities under the suppressed spin decay [10,11].

Experimental realization of the PSH state was first demonstrated using a transient spin grating technique in (001) GaAs/AlGaAs QWs [12]. A gate-controlled PSH state was realized in a (001) InGaAs/InAlAs QW through the crossover between weak localization and weak antilocalization in the quantum interference effect [13]. Furthermore, magneto-optical Kerr microscopy has enabled direct imaging of formation of the PSH state and enhancement of the spin lifetime by lateral confinement [14,15]. Recently, drift spin transport under the PSH state has been demonstrated [16] and robust spin states have also been proposed not only in (110)-grown QWs but also in other crystal orientations [17]. Consequently, the physics underlying the PSH state has been studied intensively both theoretically [8,9,17–21] and experimentally [12–16,22–25].

_____
*makoto@material.tohoku.ac.jp
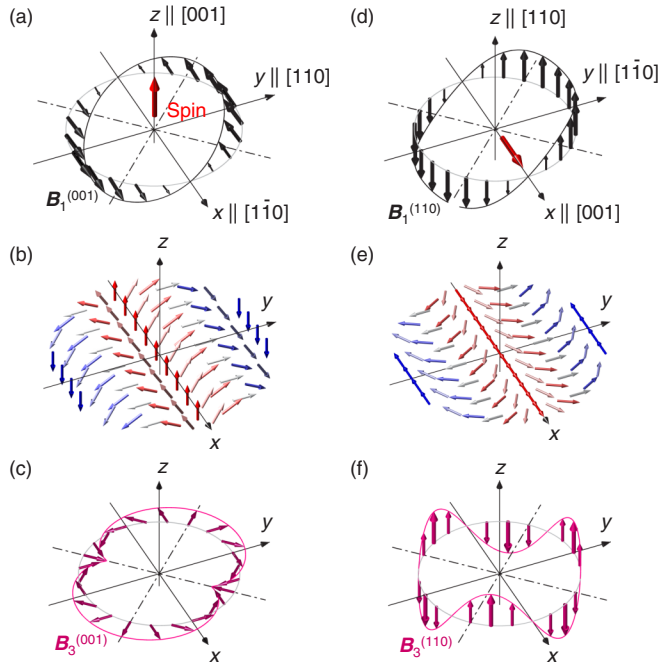
FIG. 1. Schematic illustrations of momentum-dependent effective magnetic fields in a persistent spin helix state, assuming (a) $\alpha > 0$, $\beta_1 - \beta_3 > 0$ in a (001) QW and (d) $\alpha = 0$, $\beta_1 - \beta_3 > 0$ in a (110) QW. (b, e) Helical spin textures with spins initialized along $z \parallel [001]$ in a (001) QW and $x \parallel [001]$ in a (110) QW. Helical spin textures are developed in a y-z plane in a (001) QW, whereas they are developed in a x-y plane in a (110) QW. Third angular harmonics in a cubic Dresselhaus field are shown for (c) a (001) QW and for (f) a (110) QW. A (001) QW has three rotation symmetry of the effective magnetic field with constant SO field strength, whereas a (110) QW shows uniaxial alignment along the z direction with modulated SO field strength.

Cubic Dresselhaus SO interaction influences the spin lifetime of the PSH state differently with (001) and (110) crystal orientations. Under the spin orientation initialized *parallel* to the uniaxial SO fields, although the spin orientation is randomized by the cubic Dresselhaus field in a (001) QW, long spin relaxation takes place in the case of a (110) QW because of the uniaxial alignment of both linear and cubic SO fields [Figs. 1(d) and 1(f)] [26]. Therefore, the spin state in a (110) QW is expected to be robust against cubic Dresselhaus SO interaction when compared with that in a (001) QW [27]. However, when the helical spin mode is developed by initializing the spin orientation *perpendicularly* to the uniaxial SO fields, the cubic Dresselhaus SO interaction becomes an obstacle for realizing the SU(2) symmetry [9]. It limits the spin lifetime in both (001) and (110) QWs. As shown in Figs. 1(c) and 1(f), cubic Dresselhaus fields ($\boldsymbol{B}_3^{(001)}$, $\boldsymbol{B}_3^{(110)}$) hold different symmetries between (001) and (110) QWs. Actually, $\boldsymbol{B}_3^{(001)}$ in a (001) QW shows three rotational symmetry with constant SO-field strength, whereas $\boldsymbol{B}_3^{(110)}$ in a (110) QW shows uniaxial alignment along the z direction with modulated SO-field strength. Consequently, the robustness of the PSH state with different symmetry of cubic Dresselhaus fields between (001) and (110) QWs remains elusive. However, no

quantitative comparison of the spin lifetime of the PSH state between two crystal orientations has been reported to date.

Here, we present investigation of the cubic Dresselhaus field influence on the robustness of the PSH state in (001) and (110) QWs based on a numerical Monte Carlo approach and magnetoconductance simulation, which, respectively, represent optical spin excitation/detection and weak localization (WL)/weak antilocalization (WAL) in magnetotransport. Although the magnetoconductance simulation exhibits a transition from WL to WAL against the cubic term in a (001) QW, WL is observed consistently in the case of a (110) QW, maintaining a robust spin state against the cubic term. However, in Monte Carlo simulations, we demonstrate that the lifetime of the PSH state in a (110) QW is more vulnerable to the cubic term than that in a (001) QW, being a contrast to the case of magnetotransport. By deriving the PSH lifetime in a (110) QW from a diffusion equation using a random-walk approach, we demonstrate that such a difference arises directly from the magnitude and orientation of third angular harmonics in cubic Dresselhaus fields in (001) and (110) QWs.

This paper is organized as follows. In Sec. II we explain the SO Hamiltonian and effective magnetic field symmetry in (001) and (110) QWs. Next, in Sec. III, we introduce models for establishing the spin dynamics simulation based on numerical Monte Carlo method and the magnetotransport simulation based on an efficient recursive Green's-function algorithm. In Sec. IV, we compare the simulated results for the PSH states in optical spin excitation/detection and magnetotransport. Then, the random walk model is introduced to obtain the life time of helical spin mode in (001) and (110) QWs and compare with the Monte Carlo simulation. Since cubic Dresselhaus SO fields exhibit different symmetry in (001) and (110) QWs, we focus on different spin lifetime behaviors caused by the symmetry difference in Sec. V. We close the paper with the conclusions in Sec. VI.

II. PERSISTENT SPIN HELIX STATE IN (001) AND (110) QUANTUM WELLS

For conduction electrons in a (001) QW, the Hamiltonian for an electron in $x \parallel [1\bar{1}0]$, $y \parallel [110]$, and $z \parallel [001]$ axes is described as

$$H = \frac{\hbar^2 k^2}{2m} + \frac{g\mu_{\mathrm{B}}}{2} \boldsymbol{B}_{\mathrm{SO}} \cdot \boldsymbol{\sigma}, \tag{1}$$

where in-plane wave vector $\boldsymbol{k} = (k_x, k_y)$, reduced Planck's constant $\hbar$, effective mass m, and SO field are used:

$$\boldsymbol{B}_{\mathrm{SO}}^{(001)} = \frac{2}{g\mu_{\mathrm{B}}} \begin{pmatrix} (\alpha + \beta_1 + 2\beta_3 \frac{k_x^2 - k_y^2}{k^2})k_y \\ (-\alpha + \beta_1 - 2\beta_3 \frac{k_x^2 - k_y^2}{k^2})k_x \end{pmatrix}. \tag{2}$$

In the equation above, g is the electron's g factor, μ_{B} represents the Bohr magneton, and $\boldsymbol{\sigma}$ are Pauli matrices. The magnitudes of Rashba, linear, and cubic Dresselhaus SO fields are characterized, respectively, by α, $\beta_1 = -\gamma \langle k_z^2 \rangle$, and $\beta_3 = -\gamma k^2/4$. Also, $\langle k_z^2 \rangle$ is the expected value of the wave function confined in the QW; γ is the bulk Dresselhaus coefficient, with a sign defined as negative ($\gamma < 0$). In Eq. (2), by defining θ as the counterclockwise (ccw) angle from the x axis in the x-y plane, i.e., $k_x = k\cos\theta$ and $k_y = k\sin\theta$, the effective

magnetic field is written simply by angular harmonics as

$$\boldsymbol{B}_{\text{SO}}^{(001)} = \frac{k}{g\mu_{\text{B}}}\left[\begin{pmatrix} 2(\alpha + \beta_1 - \beta_3)\sin\theta \\ 2(-\alpha + \beta_1 + \beta_3)\cos\theta \\ 0 \end{pmatrix} + \begin{pmatrix} 2\beta_3\sin 3\theta \\ -2\beta_3\cos 3\theta \\ 0 \end{pmatrix}\right]$$

$$= \boldsymbol{B}_1^{(001)} + \boldsymbol{B}_3^{(001)}. \tag{3}$$

For the PSH state in which $\alpha = \beta_1 - \beta_3$ is satisfied, as we described above, first angular harmonics $\boldsymbol{B}_1^{(001)}$ form a unidirectional effective magnetic field with SU(2) symmetry [Fig. 1(a)], protecting spins from all forms of spin independent scattering events. However, the third angular harmonics $\boldsymbol{B}_3^{(001)}$ originated from the cubic Dresselhaus field destroy the PSH state. By following the same steps for a (110) QW, the effective magnetic field $\boldsymbol{B}_{\text{SO}}^{(110)}$ is described as

$$\boldsymbol{B}_{\text{SO}}^{(110)} = \frac{k}{g\mu_{\text{B}}}\left[\begin{pmatrix} 2\alpha\sin\theta \\ -2\alpha\cos\theta \\ (\beta_1 - \beta_3)\sin\theta \end{pmatrix} + \begin{pmatrix} 0 \\ 0 \\ 3\beta_3\sin 3\theta \end{pmatrix}\right]$$

$$= \boldsymbol{B}_1^{(110)} + \boldsymbol{B}_3^{(110)}. \tag{4}$$

The coordinates for crystal directions are $x \parallel [001]$, $y \parallel [1\bar{1}0]$, and $z \parallel [110]$ in the case of a (110) QW. When the QW potential becomes symmetric, where the coefficient of Rashba SO interaction disappears ($\alpha = 0$), electron spins initially aligned along $x \parallel [001]$ or $y \parallel [1\bar{1}0]$ develop the helical spin mode and form the PSH state because of the SU(2) symmetry of $\boldsymbol{B}_1^{(110)}$ [Figs. 1(d) and 1(e)]. The induced PSH state is destroyed by third angular harmonics $\boldsymbol{B}_3^{(110)}$ [Fig. 1(f)]. Both $\boldsymbol{B}_3^{(001)}$ and $\boldsymbol{B}_3^{(110)}$ show threefold symmetry in the x-y plane, as portrayed in Figs. 1(c) and 1(f). It is noteworthy that the $\boldsymbol{B}_3^{(001)}$ strength remains constant in the x-y plane, but that of $\boldsymbol{B}_3^{(110)}$ depends on the in-plane direction. Such different symmetry of cubic SO fields affects breaking of the PSH state between (001) and (110) QWs.

III. SIMULATION MODELS FOR OPTICAL SPIN EXCITATION/DETECTION AND MAGNETOTRANSPORT

In a simple spin-diffusion model without considering the interference effect, i.e., optical pump and probe measurements of electron spins, an electron spin can be regarded as a classical spin vector [28]. We consider a degenerate electron gas with $k_{\text{B}}T \ll \hbar^2 k_F^2/2m$, where k_F is the Fermi wave number and k_{B} is Boltzmann's constant. We assume that SO splitting is slight compared to the Fermi energy and that the initial spin polarization density is lower than the electron sheet carrier density N_{s}. Then the relevant electronic states are centered at the Fermi energy. All k in equations and in definition of β_3 can be replaced by the Fermi wave number k_F. Electrons in the QWs move with Fermi velocity and experience momentum-dependent SO fields during the scattering events. Therefore, spin dynamics is governed by the following expression using $\boldsymbol{\Omega} = (g\mu_{\text{B}}/\hbar)\boldsymbol{B}_{\text{SO}}^{(001),(110)}$:

$$\frac{\partial}{\partial t}\boldsymbol{s} = \boldsymbol{\Omega} \times \boldsymbol{s}. \tag{5}$$

In our Monte Carlo simulations, electron spins $\boldsymbol{s}$ are initialized along $z \parallel [001]$ [$\boldsymbol{s} = (0, 0, S_{z0})$] in a (001) QW

and $x \parallel [001]$ or $y \parallel [1\bar{1}0]$ [$\boldsymbol{s} = (S_{x0}, 0, 0)$, $\boldsymbol{s} = (0, S_{y0}, 0)$] in a (110) QW at time $t = 0$ with a Gaussian distribution, corresponding to the optical excitation of electron spins by circularly polarized light. Wave numbers are distributed on the Fermi circle. The spot size of the excited spin distribution is defined by Gaussian sigma width as $w = 1 \, \mu\text{m}$ at time $t = 0$. We solve Eq. (5) at each discrete time step and update the spin orientation and spatial coordinate, i.e., $\boldsymbol{s}_n = (S_{x,n}, S_{y,n}, S_{z,n})$ and (x_n, y_n), where n is the increment number. Scattering events are translated as completely random variation of electron momenta to represent the proper spin-diffusion constant D_s. The spin-diffusion constant is set to $D_s = 0.012 \, \text{m}^2/\text{s}$. The sheet carrier density is $N_{\text{s}} = 5.0 \times 10^{15} \, \text{m}^{-2}$, which is related with $k_F = \sqrt{2\pi N_{\text{s}}}$. To compare robustness of the PSH state in different crystal orientations, we define the value of the SO coefficient in the PSH state as $M_{\text{PSH}} = 12 \times 10^{-13}$ eVm and set M_{PSH} as equal for both (001) and (110) QWs, i.e., $2[\alpha^{(001)} + \beta_1^{(001)} - \beta_3^{(001)}] = \beta_1^{(110)} - \beta_3^{(110)} = M_{\text{PSH}}$, corresponding to $|\boldsymbol{B}_1^{(001)}| = |\boldsymbol{B}_1^{(110)}|$. This setting gives an identical spin precession period in space when electron spins propagate with the helical spin mode. Factor 2 derives from the definition of SO fields in (001) and (110) QWs as $\boldsymbol{B}_{\text{PSH}}^{(001)} = (2k/g\mu_{\text{B}})(\alpha + \beta_1 - \beta_3)\sin\theta$ and $\boldsymbol{B}_{\text{PSH}}^{(110)} = (k/g\mu_{\text{B}})(\beta_1 - \beta_3)\sin\theta$, respectively, representing the maximum strength of the SO field in the PSH state. To elucidate the effect of the cubic term on the robustness of the PSH state, we keep M_{PSH} constant and change the magnitude of β_3 independently from M_{PSH}. Such a condition corresponds to the case of using samples that host different widths of QW [29] with appropriate carrier density because the change of QW width modulates the value of $\langle k_z^2 \rangle$, i.e., $\beta_1 = -\gamma \langle k_z^2 \rangle$, and carrier density controls α and $\beta_3 = -\gamma k^2/4$. As a result, constant M_{PSH} with different β_3 can be realized to compare the PSH state in (001) and (110) QWs. It is noteworthy that $\beta_1 - \beta_3$ in M_{PSH} is fixed as constant under the variation of β_3 in $\boldsymbol{B}_3^{(001), (110)}$.

To compare the effects of cubic terms observed in the Monte Carlo simulations, we numerically computed the magnetoconductance for disordered mesoscopic conductors using the KWANT code [30], which is based on an efficient recursive Green's-function algorithm within Landauer formalism. We consider a two-dimensional diffusive conductor with the SO Hamiltonian based on Eq. (1) in (001) and (110) QWs and calculate the total quantum transmission probability $T(E_F)$ at Fermi energy, which yields conductance in linear response within the Landauer approach: $G = G_0 T(E_F)$ (G_0 is $2e^2/h$). Also, G is computed as a function of the perpendicular magnetic field to observe WL/WAL under various $\Lambda = \beta_3/M_{\text{PSH}}$ ratios. Because of time limitations for the numerical simulation, we chose a system size and energy scales smaller than the realistic Fermi energies and set the ratio of SO parameters as comparable to the Monte Carlo simulation, which was useful for describing the SO parameter dependence in magnetoconductance [13,23]. Our KWANT simulation used the following parameters: phase coherence length $L_\varphi = 600$ nm, mean free path $L_{\text{el}} = 69$ nm, conductor width $W = 184$ nm, Fermi energy $E_F = 23.8$ meV, and g factor $g = -0.28$. We define the SO parameters normalized by hopping energy $E_h = \hbar^2/2ma^2$, where a is the lattice constant.
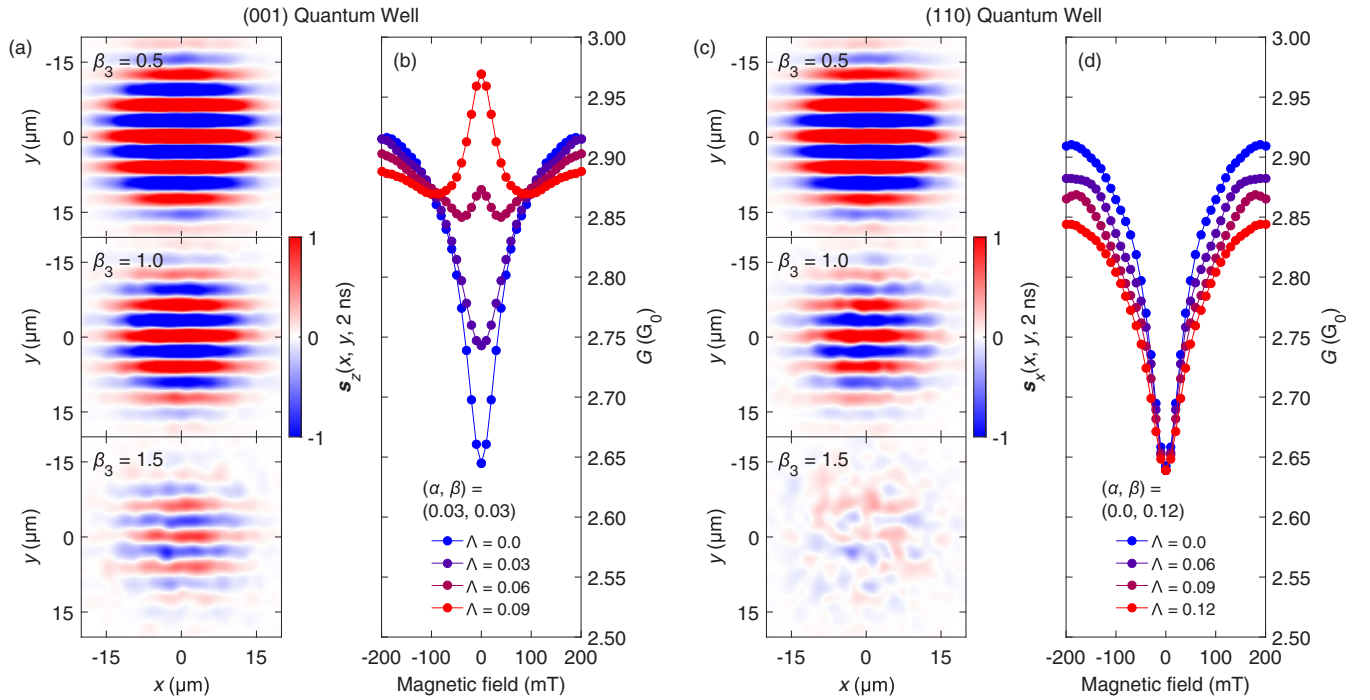
FIG. 2. (a, c) Simulated spatial maps of spin polarization for (001) and (110) QWs at time $t = 2$ ns after the spin excitation under different strengths of $\beta_3 = 0.5$, 1.0, and 1.5 (10^{-13} eV m). Red and blue colors denote the magnitude of positive and negative spin polarizations along the z (x) direction for a (001) [(110)] QW. The PSH states in both QWs are degraded as β_3 increases. (b, d) Magnetoconductance as a function of perpendicular external magnetic field calculated using recursive Green's-function method. Magnetoconductance under various values of the normalized cubic Dresselhaus term, $\Lambda = \beta_3 / M_{PSH}$, is calculated for both QWs. Crossover from WL to WAL is observed clearly in a (001) QW, although WL states are preserved entirely for a variation of Λ in a (110) QW.

IV. ROBUSTNESS OF PERSISTENT SPIN HELIX STATE

As presented in Fig. 2, we simulated a spatial map of spin polarization at $t = 2$ ns [Figs. 2(a) and 2(c)] and magneto-conductance G [Figs. 2(b) and 2(d)], respectively, under the PSH state with different β_3 and $\Lambda = \beta_3 / M_{PSH}$. In a (001) QW, WAL [red circles in Fig. 2(b)] emerges via WL (blue circles) with increasing Λ from 0 to 0.09. This result is consistent with the degraded PSH states in the Monte Carlo simulation [Fig. 2(a)] as the magnitude of β_3 increased, with induced symmetry breaking of SU(2). In contrast to a (001) QW, WL remains under strong Λ in a (110) QW [Fig. 2(d)], although the WL amplitude decreases. The preserved WL indicates a robust spin state in a (110) QW under β_3, which shows good agreement with results obtained in an earlier study [27]. However, as presented in Fig. 2(c), the helical spin mode in a (110) QW becomes more degraded by β_3 than that in a (001) QW [$\beta_3 = 1.5$ in Figs. 2(a) and 2(c)], implying a rather fragile PSH state for a (110) QW, in contrast to results of magnetoconductance simulation [Fig. 2(d)]. This implication is surprising because a (001) QW shows consistent degradation of spin states by the cubic term between Monte Carlo and magnetoconductance simulations.

To elucidate the PSH stability between (001) and (110) QWs quantitatively, we evaluate the spin lifetime by simulating the time evolution of spin polarization with different β_3 in Monte Carlo simulations. Figures 3(a) and 3(b) depict the time decay of spin polarization at the center coordinate for (001) and (110) QWs under spin excitation along $z \parallel [001]$ and $x \parallel [001]$: $s_{z,x}(0, 0, t)$ with $\beta_3 = 0$, 0.5, 1.0, and 1.5 $\times 10^{-13}$ (eVm). For the quantitative evaluation of the spin lifetime from Figs. 3(a) and 3(b), we derive the expression of the spin mode dynamics as well as the spin lifetime in a (110) QW based on a random-walk approach [19]. By consideration of the series expansion of Eq. (5) up to second order, the profile of spin polarization s at arbitrary position $\mathbf{r} = (x, y)$ and time t satisfies the following equation of motion [Appendix A presents a detailed derivation for a (110) QW]:

$$\frac{\partial}{\partial t} s(\mathbf{r}, t) = \Xi^{(110)} s(\mathbf{r}, t), \qquad (6)$$

with

$$\Xi^{(110)} = \begin{pmatrix} D_s \nabla^2 & 0 & 0 \\ 0 & D_s \nabla^2 & 0 \\ 0 & 0 & D_s \nabla^2 \end{pmatrix} - D_s \frac{m^2}{\hbar^4} \begin{pmatrix} 4\alpha^2 + (\beta^2 + 9\beta_3^2) & -\frac{2\hbar^2}{m}\beta\frac{\partial}{\partial y} & \frac{4\hbar^2}{m}\alpha\frac{\partial}{\partial x} - 2\alpha\beta \\ \frac{2\hbar^2}{m}\beta\frac{\partial}{\partial y} & 4\alpha^2 + (\beta^2 + 9\beta_3^2) & -\frac{2\hbar^2}{m}\alpha\frac{\partial}{\partial y} \\ -\frac{4\hbar^2}{m}\alpha\frac{\partial}{\partial x} - 2\alpha\beta & \frac{2\hbar^2}{m}\alpha\frac{\partial}{\partial y} & 8\alpha^2 \end{pmatrix}. \qquad (7)$$

As shown here, $\nabla^2 = (\partial^2/\partial x^2 + \partial^2/\partial y^2)$ and $\beta = \beta_1 - \beta_3$. By reflecting $\alpha = 0$ for a PSH state in a (110) QW,

$$\Xi^{(110)} = \begin{pmatrix} D_s\nabla^2 & 0 & 0 \\ 0 & D_s\nabla^2 & 0 \\ 0 & 0 & D_s\nabla^2 \end{pmatrix} - D_s\frac{m^2}{\hbar^4}\begin{pmatrix} (\beta^2 + 9\beta_3^2) & -\frac{2\hbar^2}{m}\beta\frac{\partial}{\partial y} & 0 \\ \frac{2\hbar^2}{m}\beta\frac{\partial}{\partial y} & (\beta^2 + 9\beta_3^2) & 0 \\ 0 & 0 & 0 \end{pmatrix}. \quad (8)$$

Two-dimensional Fourier transformation of Eq. (8) enables us to ascertain the solution of the spin profile in $\boldsymbol{q}$ space by the replacement of $(\partial/\partial r) \to -iq{:}\tilde{\boldsymbol{s}}(\boldsymbol{q}, t) = \int_{-\infty}^{\infty}\int_{-\infty}^{\infty}\boldsymbol{s}(\boldsymbol{r}, t)e^{-i(q_x x + q_y y)}dq_x dq_y$. By applying inverse Fourier transformation $\boldsymbol{s}(\boldsymbol{r}, t) = (1/4\pi^2)\int_{-\infty}^{\infty}\int_{-\infty}^{\infty}\tilde{\boldsymbol{s}}(\boldsymbol{q}, t)e^{i(q_x x + q_y y)}dq_x dq_y$, $\tilde{\boldsymbol{s}}(\boldsymbol{q}, t)$ returns the spin polarization along $x \parallel [001]$ in arbitrary position $\boldsymbol{r}$ as

$$\boldsymbol{s}_x(x, y, t) = S_{x0}\frac{w^2}{w^2 + 2D_s t}e^{-\frac{1}{2}\frac{(x^2+y^2)}{w^2+2D_s t}}e^{-\frac{t}{\tau_{\text{PSH}}^{(110)}}}e^{-D_s\frac{w^2}{w^2+2D_s t}q_0^2 t}\cos\left(\frac{2D_s t}{w^2 + 2D_s t}q_0 y\right), \quad (9)$$

$$1/\tau_{\text{PSH}}^{(110)} = 9D_s\frac{m^2}{\hbar^4}\beta_3^2. \quad (10)$$

In these equations, $q_0^{(110)} = m(\beta_1 - \beta_3)/\hbar^2$. Cosine oscillation in Eq. (9) shows the helical spin mode generated along the y direction because Dresselhaus SO interaction between β_1 and β_3 has a positive sign ($\gamma < 0$). $\tau_{\text{PSH}}^{(110)}$ is a spin lifetime of the PSH state in the case of a (110) QW; it is dominated by β_3.

For a (001) QW, according to [20], the spin dynamics of the PSH state at the center coordinates is governed by [Appendix B presents matrix elements in a (001) QW]

$$\boldsymbol{s}_z(0, 0, t) = S_{z0}\frac{w^2}{w^2 + 2D_s t}e^{-\frac{t}{\tau_{\text{PSH}}^{(001)}}}e^{-D_s\frac{w^2}{w^2+2D_s t}q_0^2 t}, \quad (11)$$

with

$$\frac{1}{\tau_{\text{PSH}}^{(001)}} = 6D_s\frac{m^2}{\hbar^4}\beta_3^2, \quad (12)$$

where $q_0^{(001)} = 2m(\alpha + \beta_1 - \beta_3)/\hbar^2$. We fit spin decay at the center of the PSH state in (001) and (110) QWs using Eqs. (9) and (11). The results are presented as black solid lines in Figs. 3(a) and 3(b), in which the spin dynamics in both QWs simulated by the Monte Carlo method are well described by the derived Eqs. (9) and (11), enabling us to evaluate spin lifetime $\tau_{\text{PSH}}^{(001),\ (110)}$. It is noteworthy that decay in the early time window [$t < 0.5$ ns in Figs. 3(a) and 3(b)] is attributable to terms $\exp(-D_s\frac{w^2}{w^2+2D_s t}q_0^2 t)$ and $\frac{w^2}{w^2+2D_s t}$ originating from the transition to the PSH eigenmode and diffusive dilution [20]. Figure 3(c) presents the lifetime of the PSH state in (001) and (110) QWs as a function of β_3 (filled circles and squares, respectively). We also conducted the same procedures against spins initialized along $y \parallel [1\bar{1}0]$ in a (110) QW, shown as filled triangles in Fig. 3(c), and found that the expression of spin dynamics takes the same form as that of $x \parallel [001]$ in a (110) QW. The extracted spin lifetime $\tau_{\text{PSH}}^{(110)}$ in different β_3 values clearly reflects the shorter spin lifetime of the PSH state in a (110) QW to a (001) QW. Solid lines in Fig. 3(c) correspond to theoretical results suggested by Eqs. (10) and (12), describing the evaluated $\tau_{\text{PSH}}^{(001)}$ and $\tau_{\text{PSH}}^{(110)}$ very precisely and being consistent with the spatial map of spin polarization in Figs. 2(a) and 2(c). The obtained τ_{PSH} increases quadratically as the cubic term decreases. Because β_3 is less than 1.0×10^{-13} (eVm) in typical III–V semiconductor QWs [29], the difference of the spin lifetime becomes more relevant in time for weak β_3 values.

V. ORIGIN OF DIFFERENT SPIN LIFETIME BEHAVIORS

We next consider the reason for the contrasting spin lifetime behaviors of Monte Carlo and magnetoconductance simulations in a (110) QW shown in Figs. 2(c) and 2(d). The distinct β_3 contribution to the spin-relaxation process originates from the fact that the strength of $\boldsymbol{B}_3$ dominates the randomization of spin orientation in the optical excitation, i.e., Monte Carlo method, although the direction of $\boldsymbol{B}_3$ to the
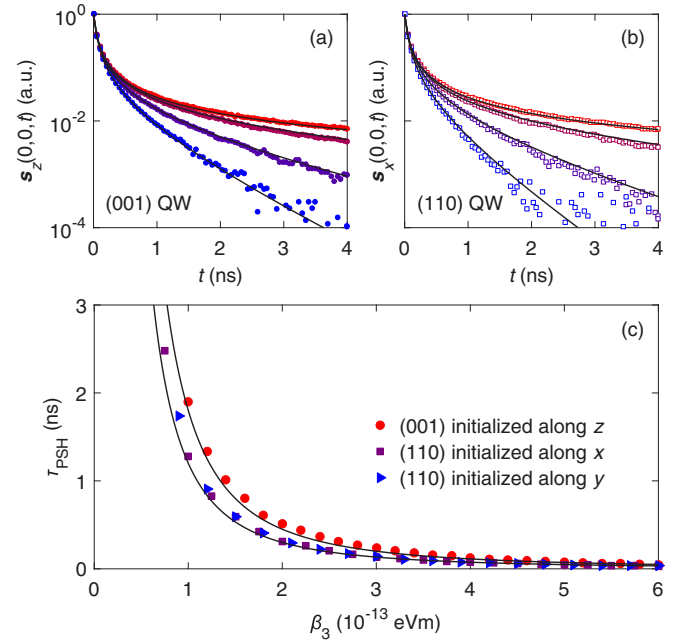
FIG. 3. Time evolution of spin polarization at coordinate $(x, y) = (0, 0)$ with different $\beta_3 = 0$, 0.5, 1.0, and 1.5 (10^{-13} eVm), respectively, in (a) a (001) QW and (b) a (110) QW. Solid lines are fitted curves using Eq. (11) for a (001) QW and Eq. (9) for a (110) QW. (c) Extracted lifetime of the PSH state under various strengths of β_3. Filled circles represent a (001) QW with spins initialized along $z \parallel [001]$. Filled squares and triangles, respectively, represent a (110) QW with spins initialized along $x \parallel [001]$ and $y \parallel [1\bar{1}0]$. Black solid lines are full calculations of the theoretical PSH lifetime [Eqs. (10) and (12)].

uniaxial SO field on the PSH state becomes more important for spin interference representing the magnetoconductance. In the random-walk approach [19,21], the spin-relaxation rates in (110) and (001) QWs shown as Eqs. (10) and (12) are derived, respectively, from the following spin decay expressions:

$$\exp\{-\langle \Omega_z^2 \rangle \tau t\},\tag{13}$$

$$\exp\{-(\langle \Omega_x^2 \rangle + \tfrac{1}{2}\langle \Omega_y^2 \rangle)\tau t\},\tag{14}$$

where Ω_i ($i = x, y,$ and z) represents the spin precession frequency by the SO field along the i direction and where τ denotes the elastic electron-scattering time. When the electron spins experience the SO fields in different paths during their diffusion [Fig. 4(b)], accumulated spin phases are mutually incoherent, with the result that the total spin precession phase is determined by the sum of Ω_i. This result reflects the expected value of the squared spin precession frequency. In such a case, the strength of $\boldsymbol{B}_3$ averaged over k space determines the spin relaxation and becomes more important than the direction of $\boldsymbol{B}_3$.

However, in the case of WL/WAL originated from the spin interference, the induced quantum correction of conductance relies on the electron propagating in a time-reversal-symmetric path [Fig. 4(a)] because of the wave nature of an electron. Resultant spin phases are oppositely accumulated because of SO fields in two partial waves for the electron propagating on the same path in the opposite direction. The expected value for the induced spin interference at the original point [R_1 in Fig. 4(a)] for clockwise (cw) and counterclockwise propagating paths is described as

$$\langle f_{\text{ccw}} | f_{\text{cw}} \rangle = \langle i_s | R^2 | i_s \rangle,\tag{15}$$

$$R = \prod_{i=1}^{n} R_i(\theta_i, \phi_i).\tag{16}$$

Here, R_i depicts the spin rotation operator between the scattering event, n corresponds to the number of scattering, θ_i and ϕ_i, respectively, denote the spin precession angles for the y and z axes, and $|i_s\rangle$ is the initial spin vector. Rotation

operator R for 1/2-spin is

$$R(\theta, \phi) = \begin{pmatrix} e^{-i\frac{\phi}{2}} \cos\left(\frac{\theta}{2}\right) & -e^{-i\frac{\phi}{2}} \sin\left(\frac{\theta}{2}\right) \\ e^{i\frac{\phi}{2}} \sin\left(\frac{\theta}{2}\right) & e^{i\frac{\phi}{2}} \cos\left(\frac{\theta}{2}\right) \end{pmatrix}.\tag{17}$$

In a general assumption under WL/WAL measurements, the spin interference takes place because of SO fields during the time-reversal-symmetric path, which depends on the SO field direction. For a (001) QW, both $\boldsymbol{B}_1^{(001)}$ and $\boldsymbol{B}_3^{(001)}$ are oriented in plane. Consequently, the spin precession angles are expected to satisfy $\theta \neq 0$ and $\phi \neq 0$. However, for a (110) QW, spin precession angles exhibit $\theta = 0$ and $\phi \neq 0$ because both $\boldsymbol{B}_1^{(110)}$ and $\boldsymbol{B}_3^{(110)}$ are perpendicular to the QW plane. By considering this, we calculate the expected value for spin interference in the time-reversal-symmetric path by taking the arbitrary initial spin orientation as well as the average over scattering angles as

$$\langle \tilde{A} \rangle = \frac{\iint_0^{2\pi} \langle i_s | R^2 | i_s \rangle d\theta d\phi}{\iint_0^{2\pi} \langle i_s | i_s \rangle d\theta d\phi},\tag{18}$$

$$|i_s\rangle = \begin{pmatrix} e^{-i\frac{\eta}{2}} \cos\left(\frac{\delta}{2}\right) \\ e^{i\frac{\eta}{2}} \sin\left(\frac{\delta}{2}\right) \end{pmatrix}.\tag{19}$$

Here, η and δ are the initial angles of a spin in the Bloch sphere. For a (001) QW, $\langle \tilde{A} \rangle$ becomes the negative value of $-1/2$, resulting in the suppression of localization, i.e., WAL. However, we obtain $\langle \tilde{A} \rangle = 0$ for a (110) QW, indicating that the spin precession does not contribute to antilocalization [31]. This general argument well explains the transition from WL to WAL in a (001) QW and the consistent observation of WL in a (110) QW under various cubic terms presented in Fig. 2. For spin interference, the direction of SO fields is significant in the time-reversal-symmetric path. Therefore, the magnitude and orientation of cubic terms contribute differently to the spin phase for incoherent and coherent scattering paths, which, respectively, describe optical excitation/detection and quantum interference on magnetoconductance.

VI. CONCLUSION

We investigated the robustness of the PSH state on the cubic Dresselhaus SO interaction in (001) and (110) QWs based on numerical Monte Carlo simulations, with comparison to the calculated quantum interference in magnetotransport. For electron spins initialized along $z \parallel [001]$ in a (001) QW and $x \parallel [001]$ and $y \parallel [1\bar{1}0]$ in a (110) QW, where the spin distribution is developed with the helical spin mode, a (001) QW shows a more robust PSH state against the increase of β_3 than does a (110) QW. This result is contrary to the numerically computed magnetoconductance, where the WL is maintained on the variation of β_3 in a (110) QW, although the WAL appears in a (001) QW. Such a difference between optical and transport properties arises from the magnitude and orientation of the cubic Dresselhaus field. Because experimental investigation of the PSH states is still in progress, our demonstration of the distinctive spin-relaxation process because of the cubic Dresselhaus field provides important insights supporting the exploration of spin-relaxation suppression as well as the

FIG. 4. (a) Time-reversal-symmetric trajectories for an electron moving clockwise (black solid arrows) and counterclockwise (pink dotted arrows) through impurity positions R_1 to R_8. During the scattering events, spins precess around the momentum-dependent spin-orbit field with opposite directions for the clockwise and counterclockwise trajectories. (b) Three independent trajectories for electrons traveling the same distance with scattering and arriving at an identical point at time t, corresponding to optically injected electrons.

application of the PSH state for future spintronics and quantum information technology.

APPENDIX A: DERIVATION FOR THE EQUATION OF MOTION TO THE HELICAL SPIN MODE IN A (110) QW

Series expansion of Eq. (5) up to second order corresponds to

$$s_{n+1} \approx s_n + \tau \boldsymbol{\Omega}_n \times s_n + \frac{\tau^2}{2} \boldsymbol{\Omega}_n \times (\boldsymbol{\Omega}_n \times s_n). \quad (A1)$$

Letting $P(\boldsymbol{r}; s)$ be the joint probability that after n steps of random walk the electron arrives at position $\boldsymbol{r}$ and letting its spin be s, the profile of magnetization at $\boldsymbol{r}$ is obtainable using the integral on the Bloch sphere:

$$\boldsymbol{m}_n(\boldsymbol{r}) = \int s P_n(\boldsymbol{r}; s) d\Sigma. \quad (A2)$$

Joint probability satisfies the recursion relation $P_{n+1}(\boldsymbol{r}) = \langle P_n(\boldsymbol{r} - \boldsymbol{v}_n\tau; s - \Delta s_n)\rangle$, leading to

$$\boldsymbol{m}_{n+1}(\boldsymbol{r}) = \langle \int s_{n+1} P_n(\boldsymbol{r} - \boldsymbol{v}_n\tau; s - \Delta s_n) d\Sigma\rangle, \quad (A3)$$

with Fermi velocity in n step, $\boldsymbol{v}_n$ and $\Delta s_n = s_{n+1} - s_n$, where $\langle \cdots \rangle$ denotes $\frac{1}{2\pi} \int_0^{2\pi} (\cdots) d\theta$. By substituting Eq. (A1) into Eq. (A3) and considering Taylor expansion up to second order again, we obtain the spin polarization profile as

$$\frac{\partial}{\partial t} s(\boldsymbol{r}, t) = \Xi s(\boldsymbol{r}, t), \quad (A4)$$

$$\Xi = \begin{pmatrix} \Xi_1 & \Xi_2 & \Xi_3 \\ \Xi_4 & \Xi_5 & \Xi_6 \\ \Xi_7 & \Xi_8 & \Xi_9 \end{pmatrix}. \quad (A5)$$

Here matrix elements are followed by $\nabla_v^2 = \langle v_x^2\rangle(\partial^2/\partial x^2) + \langle v_y^2\rangle(\partial^2/\partial y^2)$. We reread $\boldsymbol{m}$ as spin polarization s in Eq. (A4):

$$\Xi_1 = \tau\nabla_v^2 - \tau(\langle\Omega_y^2\rangle + \langle\Omega_z^2\rangle), \quad (A6)$$

$$\Xi_2 = \langle\Omega_z\rangle + 2\tau\left(\langle\Omega_z v_x\rangle\frac{\partial}{\partial x} + \langle\Omega_z v_y\rangle\frac{\partial}{\partial y}\right) + \tau\langle\Omega_x\Omega_y\rangle, \quad (A7)$$

$$\Xi_3 = \langle\Omega_y\rangle - 2\tau\left(\langle\Omega_y v_x\rangle\frac{\partial}{\partial x} + \langle\Omega_y v_y\rangle\frac{\partial}{\partial y}\right) + \tau\langle\Omega_x\Omega_z\rangle, \quad (A8)$$

$$\Xi_4 = \langle\Omega_z\rangle - 2\tau\left(\langle\Omega_z v_x\rangle\frac{\partial}{\partial x} + \langle\Omega_z v_y\rangle\frac{\partial}{\partial y}\right) + \tau\langle\Omega_x\Omega_y\rangle, \quad (A9)$$

$$\Xi_5 = \tau\nabla_v^2 - \tau(\langle\Omega_x^2\rangle + \langle\Omega_z^2\rangle), \quad (A10)$$

$$\Xi_6 = -\langle\Omega_x\rangle + 2\tau\left(\langle\Omega_x v_x\rangle\frac{\partial}{\partial x} + \langle\Omega_x v_y\rangle\frac{\partial}{\partial y}\right) + \tau\langle\Omega_y\Omega_z\rangle, \quad (A11)$$

$$\Xi_7 = -\langle\Omega_y\rangle + 2\tau\left(\langle\Omega_y v_x\rangle\frac{\partial}{\partial x} + \langle\Omega_y v_y\rangle\frac{\partial}{\partial y}\right) + \tau\langle\Omega_x\Omega_z\rangle, \quad (A12)$$

$$\Xi_8 = \langle\Omega_x\rangle - 2\tau\left(\langle\Omega_x v_x\rangle\frac{\partial}{\partial x} + \langle\Omega_x v_y\rangle\frac{\partial}{\partial y}\right) + \tau\langle\Omega_y\Omega_z\rangle, \quad (A13)$$

$$\Xi_9 = \tau\nabla_v^2 - \tau(\langle\Omega_x^2\rangle + \langle\Omega_y^2\rangle). \quad (A14)$$

It is noteworthy that v_x and v_y are the velocity components for electron spin; $\Omega_{x,y,z}$ are the corresponding components of the precession vector.

In a (110) QW, Ω_z does not disappear. The corresponding terms drop to zero, producing the matrix

$$\Xi^{(110)} = \tau \begin{pmatrix} \nabla_v^2 - \langle\Omega_y^2\rangle - \langle\Omega_z^2\rangle & 2\langle\Omega_z v_y\rangle\frac{\partial}{\partial y} & -2\langle\Omega_y v_x\rangle\frac{\partial}{\partial x} + \langle\Omega_x\Omega_z\rangle \\ -2\langle\Omega_z v_y\rangle\frac{\partial}{\partial y} & \nabla_v^2 - \langle\Omega_z^2\rangle - \langle\Omega_x^2\rangle & 2\langle\Omega_x v_y\rangle\frac{\partial}{\partial y} \\ 2\langle\Omega_y v_x\rangle\frac{\partial}{\partial x} + \langle\Omega_x\Omega_z\rangle & -2\langle\Omega_x v_y\rangle\frac{\partial}{\partial y} & \nabla_v^2 - \langle\Omega_x^2\rangle - \langle\Omega_y^2\rangle \end{pmatrix}. \quad (A15)$$

Under the PSH situation in a (110) QW, because the Rashba term α disappears, $\langle\Omega_x^2\rangle = \langle\Omega_y^2\rangle = \langle\Omega_x\Omega_z\rangle = \langle\Omega_y v_x\rangle = \langle\Omega_x v_y\rangle = 0$. Therefore calculated Eq. (A15) corresponds to Eq. (8) via Eq. (7) in the main text. Two-dimensional Fourier transformation of Eq. (A4) with a matrix for a (110) QW [Eq. (8)] enables us to ascertain the solution of the spin profile in $\boldsymbol{q}$ space as described in the main text.

APPENDIX B: MATRIX ELEMENTS FOR A (001) QW

For a (001) QW, corresponding averages vanish. Therefore,

$$\Xi^{(001)} = \tau \begin{pmatrix} \nabla_v^2 - \langle \Omega_y^2 \rangle & 0 & -2\langle \Omega_y v_x \rangle \frac{\partial}{\partial x} \\ 0 & \nabla_v^2 - \langle \Omega_x^2 \rangle & 2\langle \Omega_x v_y \rangle \frac{\partial}{\partial y} \\ 2\langle \Omega_y v_x \rangle \frac{\partial}{\partial x} & -2\langle \Omega_x v_y \rangle \frac{\partial}{\partial y} & \nabla_v^2 - \langle \Omega_x^2 \rangle - \langle \Omega_y^2 \rangle \end{pmatrix}. \tag{B1}$$

In the PSH state,

$$\Xi^{(001)} = \begin{pmatrix} D_s \nabla^2 & 0 & 0 \\ 0 & D_s \nabla^2 & 0 \\ 0 & 0 & D_s \nabla^2 \end{pmatrix} - 4D_s \frac{m^2}{\hbar^4} \begin{pmatrix} \beta_3^2 & 0 & 0 \\ 0 & [(\alpha+\beta)^2 + \beta_3^2] & -\frac{\hbar^2}{m}(\alpha+\beta)\frac{\partial}{\partial y} \\ 0 & \frac{\hbar^2}{m}(\alpha+\beta)\frac{\partial}{\partial y} & 2(\alpha^2 + \beta^2 + \beta_3^2) \end{pmatrix}. \tag{B2}$$

In this equation, $\nabla^2 = (\partial^2/\partial x^2 + \partial^2/\partial y^2)$ and $\beta = \beta_1 - \beta_3$. Therefore, the solution for a (001) QW is

$$s_z(x, y, t) = S_{z0} \frac{w^2}{w^2 + 2D_s t} e^{-\frac{1}{2}\frac{(x^2+y^2)}{w^2 + 2D_s t}} e^{-\frac{t}{\tau_{\text{PSH}}^{(001)}}} e^{-D_s \frac{w^2}{w^2 + 2D_s t} q_0^2 t} \cos\left(\frac{2D_s t}{w^2 + 2D_s t} q_0 y\right), \tag{B3}$$

where $q_0 = 2m(\alpha + \beta_1 - \beta_3)/\hbar^2$. Cosine oscillation in Eq. (B3) shows helical texture and evolves only in the y direction in contrast to a (110) QW because we consider the positive sign of α.

[1] G. Dresselhaus, Spin-orbit coupling effects in zinc blende structures, Phys. Rev. **100**, 580 (1955).

[2] E. I. Rashba, Properties of semiconductors with an extremum loop I. Cyclotron and combinational resonance in a magnetic field perpendicular to the plane of the loop, Sov. Phys. Solid State **2**, 1224 (1960).

[3] J. Nitta, T. Akazaki, H. Takayanagi, and T. Enoki, Gate Control of Spin-Orbit Interaction in an Inverted In$_{0.53}$Ga$_{0.47}$As/In$_{0.52}$Al$_{0.48}$As Heterostructure, Phys. Rev. Lett. **78**, 1335 (1997).

[4] Y. Kato, R. C. Myers, A. C. Gossard, and D. D. Awschalom, Coherent spin manipulation without magnetic fields in strained semiconductors, Nature (London) **427**, 50 (2004).

[5] T. Bergsten, T. Kobayashi, Y. Sekine, and J. Nitta, Experimental Demonstration of the Time Reversal Aharonov-Casher Effect, Phys. Rev. Lett. **97**, 196803 (2006).

[6] M. Kohda, S. Nakamura, Y. Nishihara, K. Kobayashi, T. Ono, J. Ohe, Y. Tokura, T. Mineno, and J. Nitta, Spin-orbit induced electronic spin separation in semiconductor nanostructures, Nat. Commun. **3**, 1082 (2012).

[7] M. I. D'yakonov and V. I. Perel', Spin orientation of electrons associated with the interband absorption of light in semiconductors, JETP **33**, 1053 (1971).

[8] J. Schliemann, J. C. Egues, and D. Loss, Nonballistic Spin-Field-Effect Transistor, Phys. Rev. Lett. **90**, 146801 (2003).

[9] B. A. Bernevig, J. Orenstein, and S.-C. Zhang, Exact SU(2) Symmetry and Persistent Spin Helix in a Spin-Orbit Coupled System, Phys. Rev. Lett. **97**, 236601 (2006).

[10] J. Schliemann, Colloquium: Persistent spin textures in semiconductor nanostructures, Rev. Mod. Phys. **89**, 011001 (2017).

[11] M. Kohda and G. Salis, Physics and application of persistent spin helix state in semiconductor heterostructures, Semicond. Sci. Technol. **32**, 073002 (2017).

[12] J. D. Koralek, C. P. Weber, J. Orenstein, B. A. Bernevig, S.-C. Zhang, S. Mack, and D. D. Awschalom, Emergence of the persistent spin helix in semiconductor quantum wells, Nature (London) **458**, 610 (2009).

[13] M. Kohda, V. Lechner, Y. Kunihashi, T. Dollinger, P. Olbrich, C. Schönhuber, I. Caspers, V. V. Bel'kov, L. E. Golub, D. Weiss, K. Richter, J. Nitta, and S. D. Ganichev, Gate-controlled persistent spin helix state in (In,Ga)As quantum wells, Phys. Rev. B **86**, 081306 (2012).

[14] M. P. Walser, C. Reichl, W. Wegscheider, and G. Salis, Direct mapping of the formation of a persistent spin helix, Nat. Phys. **8**, 757 (2012).

[15] P. Altmann, M. P. Walser, C. Reichl, W. Wegscheider, and G. Salis, Suppressed decay of a laterally confined persistent spin helix, Phys. Rev. B **90**, 201306 (2014).

[16] Y. Kunihashi, H. Sanada, H. Gotoh, K. Onomitsu, M. Kohda, J. Nitta, and T. Sogawa, Drift transport of helical spin coherence with tailored spin-orbit interactions, Nat. Commun. **7**, 10722 (2016).

[17] M. Kammermeier, P. Wenk, and J. Schliemann, Control of Spin Helix Symmetry in Semiconductor Quantum Wells by Crystal Orientation, Phys. Rev. Lett. **117**, 236801 (2016).

[18] M.-H. Liu, K.-W. Chen, S.-H. Chen, and C.-R. Chang, Persistent spin helix in Rashba-Dresselhaus two-dimensional electron systems, Phys. Rev. B **74**, 235322 (2006).

[19] L. Yang, J. Orenstein, and D. Lee, Random walk approach to spin dynamics in a two-dimensional electron gas with spin-orbit coupling, Phys. Rev. B **82**, 155324 (2010).

[20] G. Salis, M. P. Walser, P. Altmann, C. Reichl, and W. Wegscheider, Dynamics of a localized spin excitation close to the spin-helix regime, Phys. Rev. B **89**, 045304 (2014).

[21] G. J. Ferreira, F. G. G. Hernandez, P. Altmann, and G. Salis, Spin drift and diffusion in one- and two-subband helical systems, Phys. Rev. B **95**, 125119 (2017).

[22] J. Ishihara, Y. Ohno, and H. Ohno, Direct imaging of gate-controlled persistent spin helix state in a modulation-doped GaAs/AlGaAs quantum well, Appl. Phys. Express **7**, 013001 (2014).

[23] A. Sasaki, S. Nonaka, Y. Kunihashi, M. Kohda, T. Bauernfeind, T. Dollinger, K. Richter, and J. Nitta, Direct determination of spin-orbit interaction coefficients and realization

of the persistent spin helix symmetry, Nat. Nanotechnol. **9**, 703 (2014).

[24] P. Altmann, M. Kohda, C. Reichl, W. Wegscheider, and G. Salis, Transition of a two-dimensional spin mode to a helical state by lateral confinement, Phys. Rev. B **92**, 235304 (2015).

[25] K. Yoshizumi, A. Sasaki, M. Kohda, and J. Nitta, Gate-controlled switching between persistent and inverse persistent spin helix states, Appl. Phys. Lett. **108**, 132402 (2016).

[26] Y. Ohno, R. Terauchi, T. Adachi, F. Matsukura, and H. Ohno, Spin Relaxation in GaAs(110) Quantum Wells, Phys. Rev. Lett. **83**, 4196 (1999).

[27] T. Hassenkam, S. Pedersen, K. Baklanov, A. Kristensen, C. B. Sorensen, P. E. Lindelof, F. G. Pikus, and G. E. Pikus, Spin

[28] splitting and weak localization in (110) GaAs/Al_xGa_{1-x}As quantum wells, Phys. Rev. B **55**, 9298 (1997).

[28] A. A. Kiselev and K. W. Kim, Progressive suppression of spin relaxation in two-dimensional channels of finite width, Phys. Rev. B **61**, 13115 (2000).

[29] M. P. Walser, U. Siegenthaler, V. Lechner, D. Schuh, S. D. Ganichev, W. Wegscheider, and G. Salis, Dependence of the Dresselhaus spin-orbit interaction on the quantum well width, Phys. Rev. B **86**, 195309 (2012).

[30] C. W. Groth, M. Wimmer, A. R. Akhmerov, and X. Waintal, Kwant: A software package for quantum transport, New J. Phys. **16**, 063065 (2014).

[31] R. Berkovits and M. Kaveh, Backscattering of high-energy electrons from disordered media: Antienhancement due to the spin-orbit interaction, Phys. Rev. B **37**, 584 (1988).